4-17-2024

Achieving room temperature plasticity in brittle ceramics through elevated temperature preloading

Chao Shen
Purdue University, shen569@purdue.edu

Jin Li
Purdue University

Tongjun Niu
Purdue University, niu35@purdue.edu

Jaehun Cho
Purdue University, Cho299@purdue.edu

Zhongxia Shang
Purdue University, shang19@purdue.edu

See next page for additional authors

MATERIALS SCIENCE

Achieving room temperature plasticity in brittle ceramics through elevated temperature preloading

Chao Shen[1]†, Jin Li[1,2]†, Tongjun Niu[1], Jaehun Cho[1,3], Zhongxia Shang[1], Yifan Zhang[1], Anyu Shang[1], Bo Yang[1], Ke Xu[1], R. Edwin García[1], Haiyan Wang[1,4]*, Xinghang Zhang[1]*

Ceramic materials with high strength and chemical inertness are widely used as engineering materials. However, the brittle nature limits their applications as fracture occurs before the onset of plastic yielding. There has been limited success despite extensive efforts to enhance the deformability of ceramics. Here we report a method for enhancing the room temperature plastic deformability of ceramics by artificially introducing abundant defects into the materials via preloading at elevated temperatures. After the preloading treatment, single crystal (SC) TiO_2 exhibited a substantial increase in deformability, achieving 10% strain at room temperature. SC α-Al_2O_3 also showed plastic deformability, 6 to 7.5% strain, by using the preloading strategy. These preinjected defects enabled the plastic deformation process of the ceramics at room temperature. These findings suggest a great potential for defect engineering in achieving plasticity in ceramics at room temperature.

INTRODUCTION

Ceramics are widely used as structural materials in industry due to their superior mechanical strength, chemical inertness, electrical insulation, and thermal stability (*1*, *2*). However, the inherent brittleness limits their widespread applications (*3*–*5*). In general, most ceramic materials are brittle when tested at low-to-intermediate temperatures due to limited defects to accommodate plasticity with few exceptions (*6*–*10*). In most cases, dislocations are rarely observed in ceramics during deformation at room temperature (RT) due to the ultrahigh resolved shear stress required for the dislocation nucleation, which can be close to the theoretical shear strength for perfect crystals (*11*, *12*). The yield strength [determined by the critical resolved shear stress (CRSS) for shearing of atomic planes] is often greater than the fracture strength (tensile separation of atomic planes) (*12*). Moreover, dislocation glide is discouraged at RT as the lattice friction stress is high. In contrast, dislocations in metallic materials are mobile due to low friction stress, leading to improved plasticity. Therefore, the combination of high friction stress and obstacles for dislocation nucleation results in the brittle nature of most ceramic materials at RT. While most semiconductors and ceramic insulators are known to be brittle at low-to-intermediate temperatures, exceptions have been reported in certain ceramics, for example, $SrTiO_3$, where dislocations carry the RT plasticity (*13*). However, the plasticity starts to diminish at intermediate temperatures, leading to brittle behavior (*13*). Meanwhile, some plasticity observed in α-Ag_2S with a relatively low melting point ($T_m = 825°C$) was attributed to the weak structural and chemical bonding (*14*).

Besides the aforementioned ceramics, there have been numerous attempts to improve the deformability of ceramics, however, with limited successes (*15*, *16*). For example, plasticity has been previously reported in small-size ceramic samples under submicrometer scales, such as 1-μm micropillars and 25-nm nanowires of GaAs (*17*, *18*), as well as ZrC with dimensions smaller than 0.55 μm (*19*). Ceramic composites have been widely explored, where the ductile second phases in the matrix can deflect cracks, but they do not necessarily improve the plasticity of the ceramic matrix (*20*–*22*). Another way to enhance the deformability of certain ceramic systems is through grain refinement, where spark plasma sintering (SPS) is commonly used to achieve a compact microstructure with a small grain size (*23*–*27*). Grain boundary sliding and rotation have been introduced in multiple systems along with several demonstrations of superplasticity at high temperatures (*28*). An emerging technique, flash sintering, has been shown to produce defects in ceramics during the nonequilibrium and ultrafast sintering process and can facilitate inelastic deformability compared with conventional sintering methods (*29*–*32*). For example, flash-sintered 3YSZ has shown enhanced mechanical deformability linked to flash sintering induced dislocations and point defects in YSZ (*30*, *31*); abundant stacking faults (SFs) and dislocations have been observed in flash-sintered TiO_2, ZnO, and Al_2O_3 that are believed to be responsible for the enhanced RT deformability (*29*, *33*–*36*). However, challenges remain in the generalization and scalability of the flash sintering method as it is mostly demonstrated in oxides with ongoing efforts to improve sample uniformity and scalability (*37*–*40*). There is a great demand for more generalized approaches for improving RT deformability in a broad range of ceramics (*41*, *42*).

Despite the limited RT deformability, under elevated temperatures, ceramics can become more deformable and even ductile due to the activation of slip systems and nucleation of numerous defects. The CRSS required to initiate plastic deformation decreases at higher temperatures, allowing for the slip to occur more readily (*43*). For example, it has been reported that the CRSS of single crystal (SC) MgO· Al_2O_3 decreases by two orders of magnitude for {110} slip when temperature increases from 200° to 1900°C (*44*). Meanwhile, the CRSS of SC sapphire for both basal and prismatic slip drastically decreases at elevated temperatures following a temperature-dependent logarithmic law (*45*).

Inspired by the preexisting defects in flash-sintered ceramics and the elevated temperature deformability in ceramics, in this work, we propose a more generalized concept to improve RT plasticity in ceramics,

[1]School of Materials Engineering, Purdue University, West Lafayette, IN 47907, USA. [2]Institute of Special Environments Physical Sciences, Harbin Institute of Technology (Shenzhen), Shenzhen 518055, China. [3]School of Materials Science and Engineering, Kumoh National Institute of Technology, Gumi, Gyeongbuk 39177, Republic of Korea. [4]School of Electrical and Computer Engineering, Purdue University, West Lafayette, IN 47907, USA.
*Corresponding author. Email: hwang00@purdue.edu (H.W.); xzhang98@purdue.edu (X.Z.)
†These authors contributed equally to this work.

i.e., using an elevated temperature preloading method to artificially introduce abundant defects into ceramics and thus drastically improve their RT deformability. As illustrated in Fig. 1, during the elevated temperature preloading stage (beyond plastic yielding), numerous defects, including dislocation segments, SFs, and twins, can be introduced into the ceramic materials. These introduced defects contributed prominently to the plastic deformability of ceramics at RT. To validate this concept, we have selected TiO_2 and Al_2O_3 model systems as they are typical engineering ceramics. For example, TiO_2 has been extensively studied considering its physical, optical, electronic, and catalytic properties. A temperature-dependent study on the mechanical properties from RT to 1300°C suggests that TiO_2 starts to deform plastically above 600°C (*46*, *47*). Similarly, Al_2O_3 is a popular engineering ceramic material with a wide range of applications (*45*, *48*–*55*). Under elevated temperatures (>600°C), basal slip in the *a* direction is the preferred deformation mechanism in Al_2O_3 to accommodate some plasticity (*45*, *56*). However, at RT, little dislocation activity has been reported, and brittle failure dominates in Al_2O_3 (*48*, *49*, *53*). We conducted in situ scanning electron microscopy (SEM) compression test and detailed microstructural characterizations of the deformed pillars to examine the impact of the preloading methods on RT deformability. Our findings suggest that elevated temperature preloading can be an effective approach to enhance the deformability of ceramics at RT. This concept can be applied to a wide range of ceramics for improving their deformability at RT.

RESULTS

In situ microcompression tests of SC (001) TiO_2

SC (001) TiO_2 micropillar specimens tested at three different deformation conditions are referred to as DT1 (deformation at RT), DT2 (deformation at 600°C), and DT3 (preloading at 600°C to just beyond yielding, cooled to RT, and followed by RT compression). All deformation experiments were performed at a constant strain rate of 5×10^{-3} s^{-1}. As shown in Fig. 2, during the deformation of DT1 specimens at RT, all pillars experienced brittle failure at a strain of 3% or less at ultrahigh flow stress of nearly 8 GPa accompanied by the propagation of large cracks (Fig. 2, A to D). During the testing of the DT2 specimen at 600°C, pillars underwent plastic deformation. Shear bands emerged at 6% strain and propagated downward under successive compression to 12% strain (Fig. 2, E to H). Flow stress reached a plateau of 1.0 GPa. In contrast, during the testing of the DT3 specimen, flow stress increased continuously to ~6.5 GPa. Small serrations and multiple large load drops were observed in the stress-strain curves. Pillars deformed at RT sustained a giant strain of nearly 10% without noticeable major cracks. The in situ SEM snapshots of a representative DT3 pillar show the propagation of multiple shear bands with a dilated pillar top, while no obvious crack was detectable from the pillar surface (Fig. 2, I to L). See movies S1 to S3 for details.

Bright-field transmission electron microscopy (BF TEM) micrographs in fig. S1 (A to C) show that the DT1 TiO_2 pillar contains strain contours and scattered dislocations when deformed to $\varepsilon = 3\%$ (onset of catastrophic fracture). To investigate the influence of preloading on the RT deformability, postmortem TEM analyses were also performed on the DT2 and DT3 pillars of SC TiO_2. Numerous dislocations, as well as SF segments, were introduced near the pillar top after the DT2 specimen was plastically deformed to 2.5% strain at 600°C (Fig. 3, A to C). Meanwhile, for the DT3 specimen compressed to $\varepsilon = 5.5\%$ at RT (after 600°C preloading), the presence of several dark bands after compression suggested highly defective area, containing several SFs and dislocation networks throughout

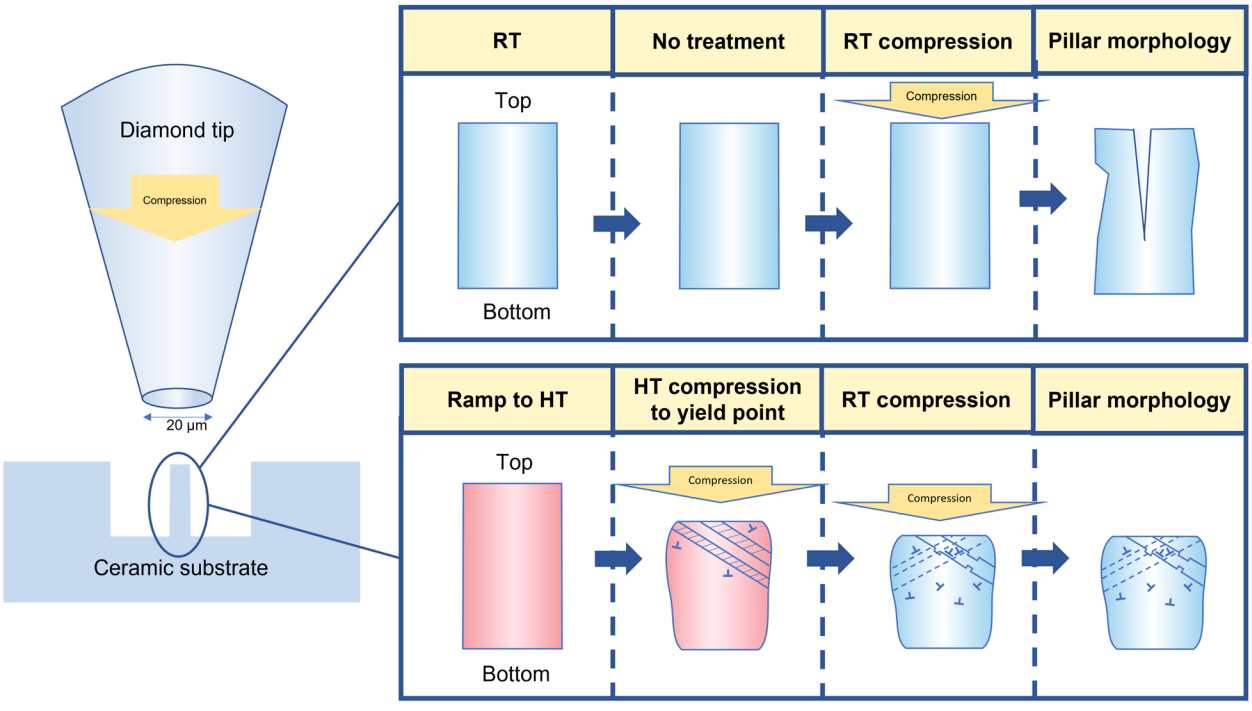

Fig. 1. Schematics of the comparison of micropillars compressed at RT with and without the treatment of preloading at elevated temperatures (the pillar top is upright). HT, high temperature.

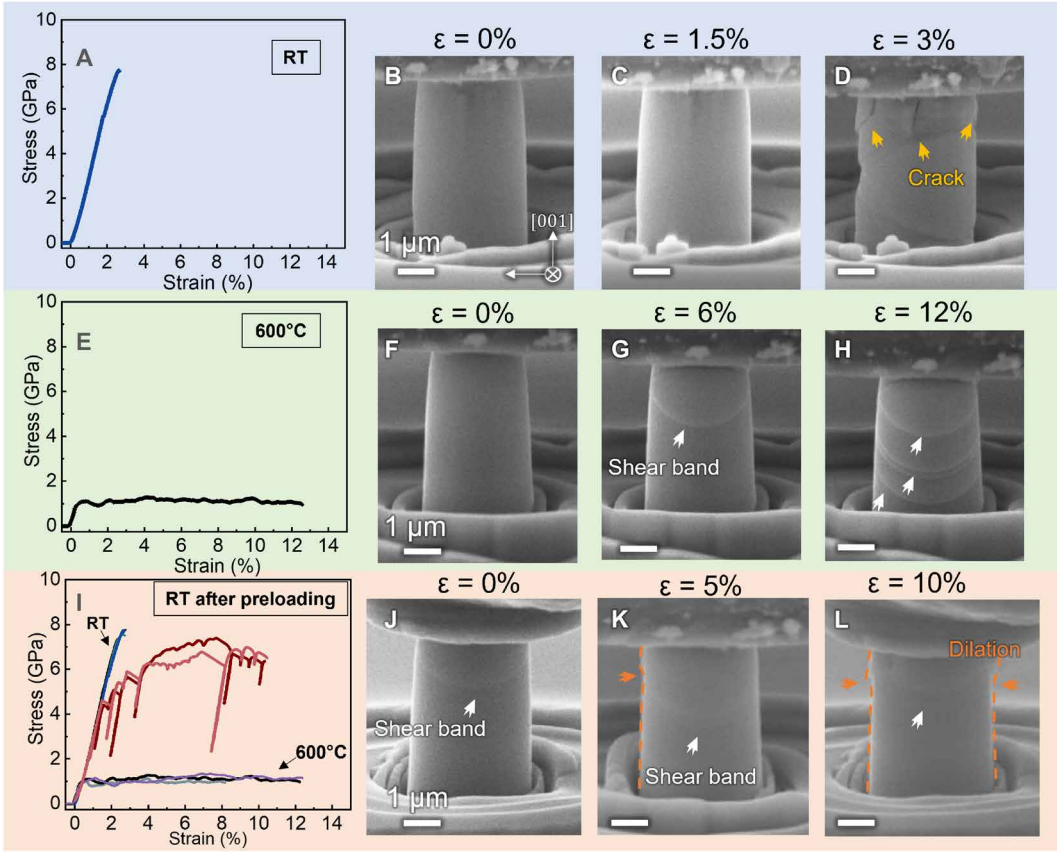

Fig. 2. Uniaxial in situ microcompression tests on the SC TiO_2 at RT, 600°C, and 600°C preloading/RT compression at a constant strain rate of 5×10^{-3} s^{-1}. (**A** to **D**) A representative stress-strain curve of SC TiO_2 tested at RT. The pillars experienced brittle failure at the strain of ~3% accompanied by the propagation of cracks. (**E** to **H**) For micropillars tested at 600°C, the shear band emerged at the strain of 6%. Evident shear bands were generated with successive compression without brittle failure. The pillar has a flow stress of ~1.0 GPa. (**I** to **L**) Micropillars were first compressed at 600°C to the yield point and cooled to the RT. During the RT compression test, flow stress increased continuously to 6.5 GPa, accompanied by serrations and load drops. Shear bands were generated, and the compressive strain reached 10% without brittle failure.

the entire pillar (Fig. 3D). The slip bands contained abundant dislocations and SFs and became broader while propagating from the upper left corner to the lower right portion of the pillar top.

Meanwhile, these dislocation-rich slip bands intersected and blocked the propagation of microcracks. When the DT3 pillars were compressed to an even greater strain, 11%, several phenomena were observed. First, in addition to the inclined microcracks, vertical microcracks appeared (Fig. 3E and fig. S2A). These microcracks were, however, terminated at ~1 μm from the pillar top surface by dislocation bands (Fig. 3D). Second, crack deflection occurred at the intersection between vertical cracks and dislocation bands. The inclined microcracks were decorated by high-density dislocation bands as well as some SFs (fig. S2, B and C) and propagated to the lower right portion of the pillar to a depth of 2 μm (or 33% of the entire pillar height). Third, grain fragmentation (labeled by arrows in Fig. 3F) was observed near the middle section of the deformed pillar, leading to subgrains with small grain sizes, as evidenced by polycrystalline selected-area electron diffraction pattern in fig. S2D. The BF TEM image and inverse pole figure (IPF) map exhibit the formation of subgrains with minor grain rotation (fig. S2, E and F). The Kernel average misorientation (KAM) map indicates a high degree of misorientation (fig. S2G), and the formation of some low-angle grain boundaries was observed near the subgrains (fig. S2H).

In situ microcompression tests of SC (0001) Al_2O_3

To explore the general applicability of the concept of preloading improved plasticity in ceramics, similar preloading experiments were performed in SC Al_2O_3. In this case, SC (0001) Al_2O_3 specimens were tested at three deformation conditions, referred to as DA1 (deformation at RT), DA2 (deformation at 740°C), and DA3 (preloading at 740°C to slightly beyond plastic yielding, cooled to RT, followed by RT compression) specimen, at a constant strain rate of 5×10^{-3} s^{-1}. As shown in Fig. 4A, during the RT deformation of the DA1 specimens, all pillars fractured at the strain of 3 to 4%, reaching a high fracture strength of ~8 GPa. In situ SEM micrographs in Fig. 4 (B to D) show that catastrophic failure and giant cracks completely disintegrated the pillar. During the deformation of DA2 pillars at 740°C, the flow stress reduced drastically to 1 GPa accompanied by serrations (Fig. 4E). In situ SEM snapshots (Fig. 4, F to I) showed that the pillars plastically deformed prominently as evidenced by the dilation of pillar top without crack when $\varepsilon \leq 6\%$. Microcracks emerged when $\varepsilon = 7\%$, and few microcracks were visible on the pillar surface when $\varepsilon = 12$ to 13% (Fig. 4, J and K). In

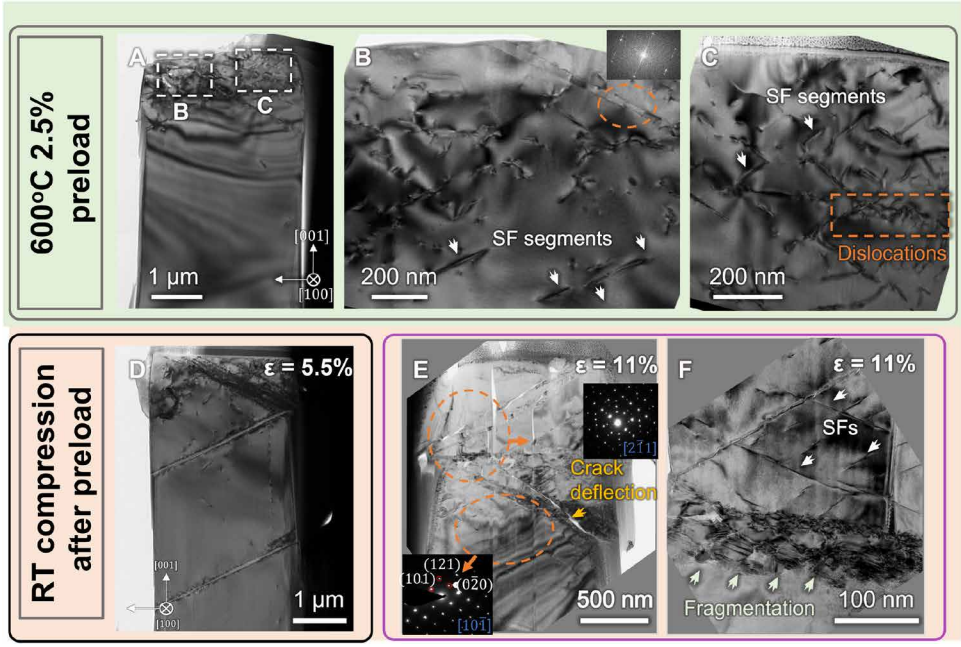

Fig. 3. TEM micrograph showing defects formation in SC TiO_2 micropillar after elevated temperature preloading and elevated temperature preloading/RT compression. (All the pillar top is upright). (**A**) Low-magnification TEM micrograph of a pillar preloaded to 2.5% strain at 600°C. A high density of dislocations nucleated on the pillar top. (**B** and **C**) Magnified TEM images from the [100] zone axis shows high-density dislocations. (**D**) Low-magnification TEM micrograph of a pillar compressed to ~5.5% strain at RT after elevated temperature preloading. Shear bands formed throughout the entire pillar. A higher density of defects was generated near the pillar top compared to the pillar bottom. (**E** and **F**) TEM micrograph of a pillar compressed to ~11% strain at RT after elevated temperature preloading. A portion of the SC TiO_2 on the bottom half of the pillar underwent grain fragmentation.

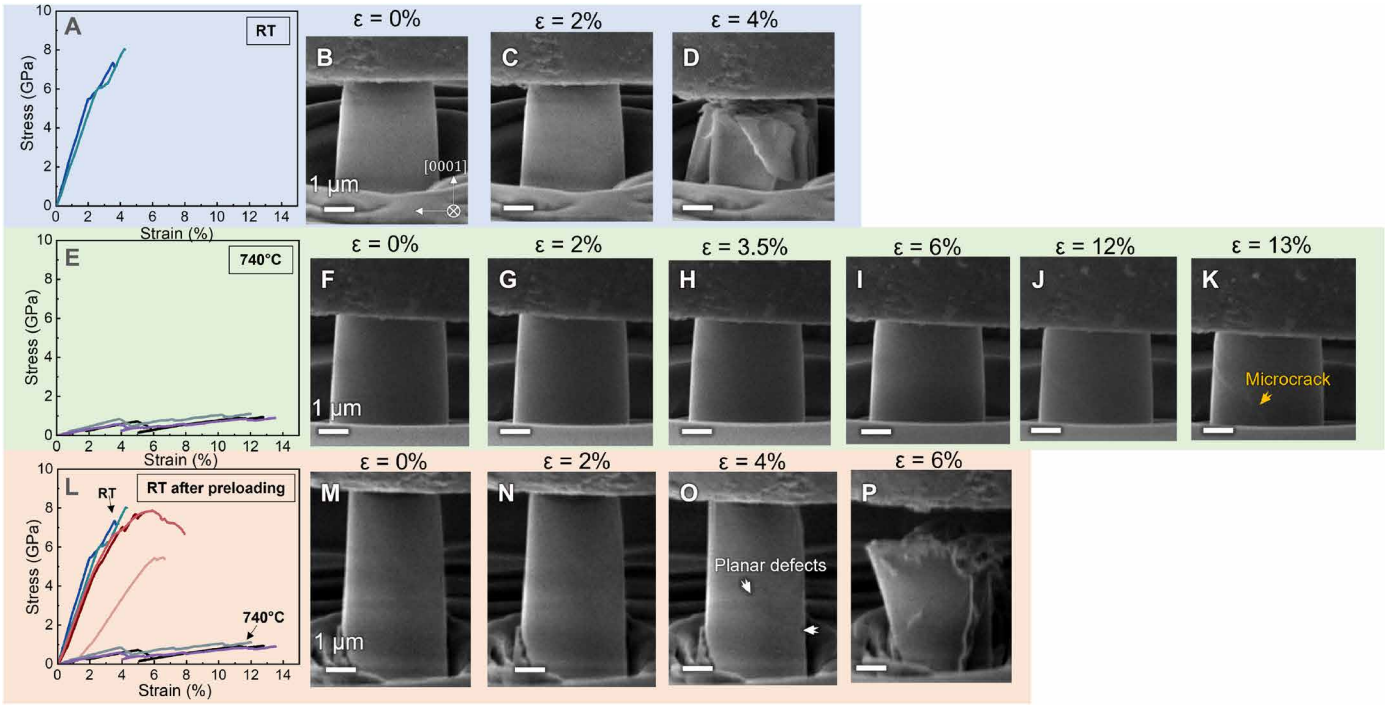

Fig. 4. Uniaxial in situ microcompression tests on the SC Al_2O_3 at RT, 740°C, and RT compression after elevated temperature preloading at a constant strain rate of 5×10^{-3} s^{-1}. (**A** to **D**) A representative stress-strain curve of SC Al_2O_3 tested at RT. SEM snapshots show that the pillars experienced a catastrophic brittle failure at the strain of 4% throughout the entire pillar. (**E** to **K**) For micropillars tested at 740°C, cracks initiated at a strain of ~7%. The pillar has a flow stress of 1 GPa at a strain of 12%. (**L** to **P**) Micropillars were first preloaded at 740°C to the yield point and cooled to the RT to continue the RT compression test. Many microcracks were generated under further RT loading. The pillar experienced failure at a strain of 6%.

comparison, the DA3 pillar reached a flow stress of 4.5 to 8 GPa and a fracture strain of 6 to 7.5% (Fig. 4L). Cracks were not observed in the pillar deformed to a strain of 4% (Fig. 4, M to O). Microcracks then propagated gradually and slowly in the lower half of the pillar until the pillar fractured when ε = 6% (Fig. 4P). See movies S4 to S6 for details.

Figure S3 shows that the SC Al_2O_3 DA1 pillar deformed at RT to a maximum fracture strain of 3% without any preloading treatment. The BF TEM images in fig. S3 (A and B) show short dislocation segments scattered in the upper half of the pillar, while some giant transgranular cracks propagated throughout the entire pillar. The IPF map in fig. S3C indicates that the crack penetration to the pillar interior leads to a minor texture change and little crystal rotation. The KAM map indicates scattered dislocations as shown in fig. S3D. The geometrically necessary dislocation (GND) map in fig. S3E shows that GNDs were mostly distributed near the pillar top and along the cracks.

Postmortem microstructure analyses were performed on the SC Al_2O_3 DA2 and DA3 micropillars to investigate the influence of preloading on the microstructure evolution. As shown in BF TEM micrographs in Fig. 5 (A and B) for the DA2 pillar preloaded to the strain of 2% at 740°C, multiple parallel $[1\bar{1}20]$ rhombohedral twins formed and extended to a depth of 3 μm from the pillar top. The high-resolution TEM micrograph in Fig. 5C shows that the twin boundary was decorated with SFs. The corresponding high-resolution IPF map (with a spatial resolution of 6 nm captured from NanoMegas ASTAR procession electron diffraction) in Fig. 5D confirms the formation of numerous nanotwins with thickness varying from 13 to 45 nm. Furthermore, the high-resolution IPF map shows that these twin boundaries are defective, as indicated by serrated steps on twin boundaries (fig. S4A). The KAM map indicates that a high degree of misorientation happened near the pillar top (fig. S4B). Meanwhile, GNDs mostly formed near the pillar top and along the

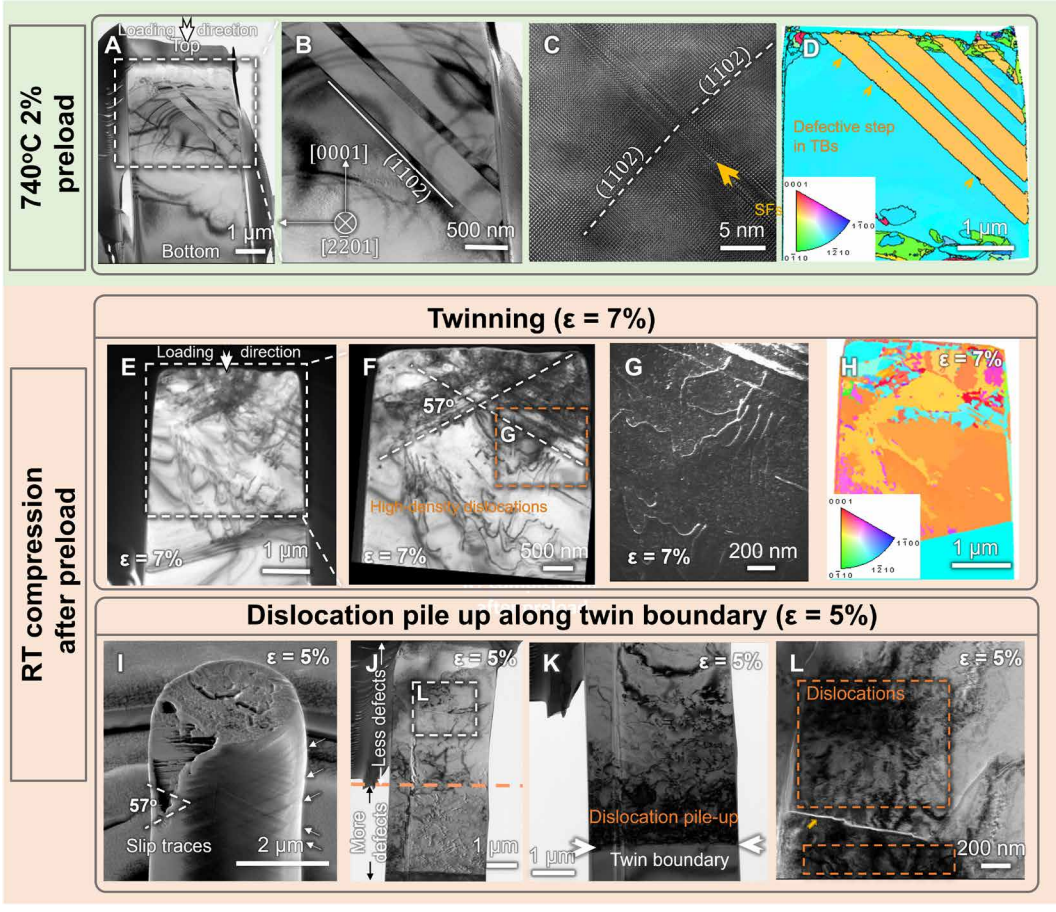

Fig. 5. TEM and SEM micrograph showing defects formation in SC Al_2O_3 micropillar after elevated temperature preloading and elevated temperature preloading/RT compression (the pillar top is upright in all images, and the compression direction is from pillar top to the bottom). (**A**) A BF TEM micrograph of the micropillar shows the formation of twin boundaries from the top left corner to the middle. (**B**) A magnified TEM image of the parallel twin boundaries. (**C**) A high-resolution TEM micrograph shows the twin boundary decorated with SFs. (**D**) The corresponding IPF exhibits the defective twin boundaries with serrated steps. (**E**) Low-magnification TEM micrograph of a pillar compressed to ~7% strain at RT after elevated temperature preloading showing the intersection of two slip bands. (**F**) A magnified TEM image of the high-density dislocations formed near the pillar top and the middle of the pillar. (**G**) A DF TEM micrograph showing the dissociation of full dislocations into two partials. (**H**) An IPF exhibiting some subgrain rotation near the pillar top. (**I**) SEM micrograph shows a pillar compressed to 5% with a dilated top, and the intersected twin boundaries appeared on the peripheral surface. (**J** and **K**) The BF TEM micrograph shows more dislocations concentrated near the twin boundary located at the pillar bottom. (**L**) The BF TEM micrograph shows that a deflected microcrack was decorated with a high density of dislocations.

twin boundaries (fig. S4C). For the DA3 pillar that underwent deformation to a strain of 7%, abundant dislocations were observed (Fig. 5E). BF TEM micrograph in Fig. 5F shows that two groups of SFs intersected with each other. Meanwhile, a high density of wavy dislocations was generated and interacted with the SFs, as shown in the dark-field (DF) TEM micrograph in Fig. 5G. The IPF map in Fig. 5H composes two similar colors as Fig. 5D, where blue is the matrix and orange represents the plastically deformed region due to twinning. The IPF map shows that a large portion of the entire pillar has undergone substantial plastic deformation. The deformed region has expanded to 2 to 3 μm from the pillar top. Nontwin orientation region was also detected, indicating local crystal reorientation. SEM image of another pillar compressed to 5% strain in Fig. 5I shows a dilated pillar top, and the intersected slip bands appeared on the pillar surface. The SEM image from a different viewing angle in fig. S5 (A to D) shows the slip trace intersection, and the rhombohedral twins block the crack propagation. The BF and DF TEM micrographs of the deformed pillar in Fig. 5 (J and K) and fig. S6 (A and B) also show a high density of dislocations concentrated, however, near a twin boundary located at the lower portion of the deformed pillar. The BF TEM micrograph in Fig. 5L shows an inclined microcrack that has propagated nearly horizontally and was decorated with a high density of dislocations. Meanwhile, a deformation-induced plastic zone was observed in front of the intersected crack tip, as shown in fig. S6C.

DISCUSSION

Our micropillar compression studies show that SC TiO_2 experienced brittle failure when tested at RT. The poor deformability of the pristine pillar is a result of the aforementioned lack of capability for the nucleation and glide of dislocations. Unexpectedly, substantial plasticity was observed in the preloaded pillar under RT compression, where the pillars were plastically deformed to 10% strain without catastrophic failure (Fig. 2I). Meanwhile, shear bands and the dilation of pillar tops were observed (Fig. 2, K and L). Similar phenomena were present in Al_2O_3, which is known for its brittle behavior at RT. At RT, the SC Al_2O_3 pillars underwent catastrophic failure at 4% strain. However, after the preloading treatment, a prominent improvement in plasticity was observed. For instance, the pillars remained intact when $\varepsilon = 4\%$ and fractured at 6%. Both studies suggest that the preloading treatment is sufficient to drastically improve the RT plasticity of brittle ceramic materials. The mechanisms behind the improved plasticity in these ceramic materials will be discussed next.

Defect-assisted RT plasticity in preloaded SC TiO_2

Compared to pristine ceramics with few defects, abundant defects, such as dislocation seeds and twin boundaries, were introduced in the pillars during the preloading at elevated temperatures. These defects allow ceramics to bypass the large CRSS required for dislocation nucleation at RT; therefore, when the preloaded pillars containing dislocations were deformed at RT, plastic deformation took place.

It has been reported that under the uniaxial compression along [001] direction between 300° and 1300°C, SC TiO_2 deformed by $\{10\bar{1}\}<101>$ slip, but no plasticity in SC TiO_2 has been reported at RT to date (*46*, *47*). In the current study, subgrains appeared after RT deformation, and dislocations were generated within one subgrain as shown in fig. S1. In comparison, numerous dislocation seeds were introduced into the SC TiO_2 pillar after being compressed at 600°C during the preloading stage as shown in Fig. 3 (A to C). Given that the compression axis of the rutile SC TiO_2 is along [001] direction and the calculation of the largest resolved shear stress, dislocations could have a Burgers vector of <101> as widely reported previously (*46*, *47*). Meanwhile, SF segments were observed near the pillar top. Once the preloaded TiO_2 pillar was further deformed at RT, the scattered dislocation seeds and SF segments aligned and propagated along the easy slip systems, leading to slip bands and SF ribbons. These dislocation activities accommodate the plasticity manifested as the dilation of the pillar top.

Work hardening is frequently observed in ductile metallic materials due to the formation of forest dislocations. In contrast, work hardening is rare in ceramics, especially at RT due to the aforementioned brittle nature of ceramics. Hence, it is unexpected that the preloaded TiO_2 pillars show a prominent work hardening phenomenon as shown in Fig. 2I. After careful examination of TEM micrographs in TiO_2 pillars deformed to a strain of 5.5% (Fig. 3, D and E), we found that upon successive loading, more dislocations and SFs were generated on inclined/intersecting slip planes. The intersection of slip bands has several consequences. First, slip bands due to the formation of high-density dislocations or SFs form barriers for the transmission of dislocations on inclined slip systems (*57*–*62*). Prior studies show that the SFs can intercept the transmission of dislocations and contribute to strengthening and prominent work hardening in metallic materials (*57*, *59*, *60*, *63*–*68*). Second, the intersection of inclined SFs leads to immobile dislocations, such as Lomer dislocations, and these sessile dislocations increase the barrier for the migration of partials and consequently increase the work hardening rate (*57*, *58*, *62*, *69*). Apart from the strengthening effect, one of the key mechanisms for SF-induced plasticity is attributed to the defaulting process where dislocations can glide along SFs, leading to substantial plasticity (*57*). Upon substantial gliding of dislocations along SFs in the same direction, shear bands may emerge. Recently, Li *et al.* (*32*) reported RT plasticity in flash-sintered polycrystalline TiO_2, and they showed that the test temperature prominently changes the deformation mechanisms and stress-strain behavior. At RT, deformation induces abundant SFs with nanoscale spacing. However, only moderate work hardening was observed (*32*). In this case, different work hardening may arise from the difference in dislocation density. It is observed that more dislocation seeds nucleated in addition to the SFs in the preloaded TiO_2 compared to the flash-sintered TiO_2. Such a high defect density in preloaded specimens may lead to more interactions between dislocations and SFs and a greater working hardening ability than the flash-sintered TiO_2.

Next, we examine the influence of dislocation slip bands on crack propagation in ceramics. Cracking is a prevalent deformation mechanism in ceramics when deformed at RT. Microcracks were also observed in TiO_2 pillars deformed to a strain of 5.5%. Figure 3E shows that some of the microcracks were blocked by intersecting slip bands. It is likely that the intersection of slip bands generated the stress localization at the intersection, which initiated the microcrack formation along the slip bands and at the intersections (*70*, *71*). The blockage of microcracks by dislocation slip bands is another evidence of improved plasticity in TiO_2 pillars deformed at RT.

In addition to work hardening and blockage of microcracks, another deformation mechanism may have also been triggered to improve RT plasticity in TiO_2. As shown in Fig. 3 (E and F), at even

greater plastic strain, 11%, many microcracks emerged, and they occurred along planes that have experienced large shear strains (evidenced by residual dislocations near the microcracks). Some of the inclined microcracks appeared to encounter each other and changed their propagation path to either vertical or lateral directions. At some of the microcrack intersected regions, grain fragmentation took place. These subgrains were isolated by the obvious slip bands or microcracks, as shown in Fig. 3F and fig. S2 (E and F) (*72*).

Defect-assisted RT plasticity in preloaded SC Al_2O_3

Similarly, the preloading concept appears effective at improving the RT plasticity of SC Al_2O_3. Some parallel rhombohedral twin boundaries as well as dislocation seeds were embedded into SC Al_2O_3 during elevated temperature preloading to 2% strain as shown in Fig. 5 (A to D). In [0001] SC Al_2O_3, it was reported that twinning stress for rhombohedral twins is constant, ~12.6 MPa, between 900 and 1373 K when the mechanical loading is parallel to the *c* axis, while twinning stress rapidly increases as the temperature decreases below 900 K (*73*). A zonal dislocation mechanism was proposed to explain the preference for rhombohedral twins over dislocation slip (*74*). As the fault energy caused by the partials in the oxygen lattice is too high, the dissociation of colinear partials 1/6 $<0\bar{1}11>$ is suppressed. Consequently, the dissociation to a zonal partial with Burgers vector of 1/21.9 $<0\bar{1}11>$ is preferred, which activates the formation of rhombohedral twins (*74*). A competing theory of shuffling mechanism may explain the formation of rhombohedral twins as well. Interfacial dislocations at the coherent twin boundaries form steps that promote twinning or detwinning. The glide of interfacial dislocations followed by shuffling in every five-atom group (consisting of two Al and three O atoms) leads to the formation of rhombohedral twins upon mechanical loading (*49*).

It should be noted that the IPF map (Fig. 5D and fig. S4) shows that the nanotwins (labeled in orange color) introduced in preloaded SC Al_2O_3 have thickness varying from tens to hundreds of nanometers. Furthermore, the high-resolution IPF map also shows numerous steps on the coherent twin boundaries. Defective twin boundaries have been observed in nanotwinned metals, and these steps consist of mobile Shockley partials that promote plasticity in nanotwinned metals (*75*–*81*).

Once the preloaded pillar was further compressed to 7% strain at RT, two sets of inclined SFs were observed to intersect with each other (Fig. 5, E and F). Such a phenomenon is similar to the intersecting defects observed in SC TiO_2 DT3 specimen preloaded and then deformed at RT (Fig. 3, D and E). DF TEM micrograph in Fig. 5G also reveals curved dislocations, indicating the activation of full dislocations in SC preloaded Al_2O_3 during deformation at RT. The weak-beam, DF TEM micrographs indicate that the dislocations in DA3 have two possible Burgers vectors, namely, $<10\bar{1}1>$ and 1/3 $<02\bar{2}1>$ (fig. S7). In this case, the possible slip systems are $\{01\bar{1}2\}/<10\bar{1}1>$ and $\{01\bar{1}2\}$ / 1 / 3 $<\bar{2}021>$, in good agreement with previous findings (*53*, *82*).

Comparing to the IPF map in preloaded SC Al_2O_3 (to a strain of 2% at 740°C) in Fig. 5D, the orange-colored region in the RT deformed preloaded specimens to 7% strain (Fig. 5H) occupied nearly the entire pillar top. Such an observation suggests that twinning remains one of the dominant deformation mechanisms. The propagations of partials on defective twin boundaries were intense enough to change the orientation of the matrix to the twin variant. Such a notable twinning process leads to prominent RT plasticity. For some dislocations that nucleated in the matrix during preloading, when they glide on the twin boundaries under shear stresses, detwinning can also take place, leading to the formation of steps on the twin boundaries (*83*–*85*). It is also possible that the defective twin boundaries act as a source to emit some mobile dislocations which prefer to glide on the planes that are inclined with respect to twin boundaries (*57*, *75*). The interaction of partials on intersecting twinning planes can result in Lomer-lock, leading to strengthening or work hardening (*57*). The work hardening phenomenon, although not as prominent as those in TiO_2, has indeed been observed in SC Al_2O_3 as shown in Fig. 4L.

Another dislocation-enabled plasticity mechanism has been observed in SC Al_2O_3. After the preloaded SC Al_2O_3 is deformed at RT to a strain of 5%, evident dilation of the pillar top was observed, and slip traces from two intersecting twin planes were also revealed on the pillar surface (Fig. 5I and fig. S5, A to D). Counterintuitively, abundant dislocations were observed near the lower portion of the deformed pillar, whereas the dilated pillar top contains fewer dislocations, as shown in fig. S6. The migration of partials along twin boundaries will lead to the exit of these partials from pillar surfaces, leaving behind slip traces. Such an exhaustion of dislocation by deformation of SC pillars has been observed in metallic materials, and the phenomenon is referred as to mechanical annealing or deformation-induced depletion of dislocations in SCs due to the free surface effect (*86*–*89*). The remaining dislocations in the pillar propagate downward driven by continuous loading. These dislocations were clearly obstructed by the twin boundary existing at the lower portion of the pillar. Such a twin boundary barricades the propagation of dislocations, leading to their pile-up (Fig. 5K). Therefore, the dislocation density is high near the twin boundary (Fig. 5K).

While the influence of preloading on nucleation of dislocations has been confirmed in this study on two model systems, TiO_2 and Al_2O_3, the mobility of dislocation is also curtailed by lattice friction stress. The substantial RT plasticity observed in preloaded TiO_2 and Al_2O_3 implies that the lattice friction stress in these ceramics may have been reduced. Several factors may play an important role. First, partial dislocations are prevalent in the deformed TiO_2 and Al_2O_3. It is known that the friction stress for partials is lower than perfect dislocations because the dislocation core width is broader for partials (*90*). Second, our ASTAR IPF studies show that twin boundaries in preloaded Al_2O_3 have steps. Such defective twin boundaries have been shown to be the source for mobile partials and thus enable prominent plasticity in twinned metallic materials (*75*). Third, it has been shown that the dislocation core in Al_2O_3 can be nonstoichiometric (*91*). Edge dislocation can dissociate into two partials on adjacent glide plane and thus improve the mobility of dislocations at elevated temperatures (*91*). It is likely that such unique dislocation cores created during preloading at elevated temperatures have been preserved at RT and thus enable the dislocation mobility at RT. RT plasticity has been reported in flash-sintered polycrystalline TiO_2 by Li *et al.* (*32*). Flash sintering, a nonequilibrium sintering technique, introduces abundant dislocations as well as oxygen vacancies during the sintering process. These defects can accommodate mechanical deformation and improve plasticity at RT. In flash-sintered ceramics, it is likely that oxygen vacancies and other charged point defects have reduced the friction stress for migration of dislocations. Similarly, It was reported that the ductility of the ferroelectric oxides

$Pb(In_{1/2}Nb_{1/2})O_3$-$Pb(Mg_{1/3}Nb_{2/3})O_3$-$PbTiO_3$ can be improved by introducing more oxygen vacancies into the system, where the covalent bonding was markedly weakened (*92*). Oxygen vacancies could also be introduced during the preloading stage under elevated temperatures and the vacuum condition in the SEM chamber. Considering our testing conditions, i.e., the temperature of 600°C for 30 min under the vacuum of 1×10^{-6} torr, the estimated diffusion length is much less than 0.4 μm. Thus, such oxygen vacancy effects could be mostly on the surface but not on the entire pillar properties. In this case, the oxygen vacancies play a minor role comparing to those of high-density dislocations and SFs observed in the preloaded pillars. Compared to flash sintering, the preloading concept is more general and can be widely used in a broad range of ceramic materials, including those that cannot be easily flash sintered.

Furthermore, to demonstrate the potential of the preloading method on improving the deformability of polycrystalline ceramics, similar preloading experiments were performed on a polycrystalline TiO_2 bulk sample prepared by SPS. Larger pillars with ~7 μm in diameter and a height of 14 μm (a diameter-to-height aspect ratio of ~1:2) were fabricated from the sample. On the basis of the preliminary data in fig. S8, it is obvious that the as-processed SPS TiO_2 pillars were brittle when tested directly at RT, and the specimens fractured instantaneously and catastrophically. Micropillar compression tests at 600°C show substantial plasticity. In comparison, subsequent RT compression tests on the preloaded pillars have endured a few percent of plastic strain before fracture, indicating that the preloading treatment also improves the RT plasticity of the polycrystalline bulk samples. In this case, the orientation effects and size effects on the improved plasticity are considered to be minimal. Such studies suggest that the preloading concept may be further scaled up to produce bulk ceramics or specific sections of large specimens and parts with prominent RT plasticity.

This work demonstrates that defects can be introduced into the ceramics through preloading treatment under elevated temperatures for improving the RT deformability of high temperature ceramics. It is important to note that selecting an appropriate preloading temperature is crucial. If the temperature is below the brittle-to-ductile transition temperature, then defects, including dislocations and SFs, will not form and thus will not improve the RT plasticity. However, if the preloading temperature is too high, some of the defects induced during preloading could be eliminated through annihilation process, reducing the impact of the preloading experiments on plasticity.

In conclusion, this study presents the concept that RT plasticity in ceramics can be achieved by introducing mobile dislocations through an elevated temperature preloading approach. The in situ micropillar compression tests indicate that the SC TiO_2 and SC Al_2O_3 can achieve substantial plasticity at RT if high-density defects were introduced during the elevated temperature preloading. These preloading-introduced mobile dislocations also allowed us to observe several interesting plastic deformation mechanisms at RT in ceramics, including the migration of SFs and twin boundaries and work hardening through the interaction of these defects, a tribute that has long been the privilege of ductile metallic materials. Introducing the preloading concept to bulk polycrystalline ceramics, as the preliminary data demonstrated, could present great potential toward future designs of bulk ductile ceramics.

MATERIALS AND METHODS

Micropillar compression test

Micropillars of SC (001) TiO_2 and SC (0001) Al_2O_3 with a dimension of ~3 μm in diameter and ~6 μm in height (a diameter-to-height aspect ratio of ~1:2) were fabricated using a focused ion beam in a Thermo Fisher Scientific Quanta 3D FEG SEM. A series of decreasing currents were used to mill the pillar with the least tapering angles in a concentric and annular crater. In situ SEM micropillar compression experiments were performed inside the Quanta 3D FEG microscope using a Hysitron PI 88 × R PicoIndenter to collect the force-displacement data. For elevated temperature in situ compression setups, the 20-μm-diameter diamond flat punch was fixed on the probe heater, and the specimens were clamped on a ceramic heating stage tightly by V-shaped molybdenum. Before the compression test, the temperature on both the heating stage and probe heater was simultaneously ramped up at a rate of 10°C/min and isothermally stabilized for 30 min to eliminate the thermal-driven drifts. An average drift rate of less than 0.5 nm/s and an estimated force noise level of less than 8 μN were monitored during the alignment preloading process for 45 s. When the temperature of both sample stage and indenter tip reached the preset values and remained stable for 30 min, preloading compression began by compressing the pillar using a diamond flat punch tip at a constant strain rate of 5×10^{-3} s^{-1}. The selection of the strain rate was within the range of the typical quasistatic uniaxial compression test. Upon detecting the yielding phenomenon from the load-displacement curve (typically at a plastic strain of 2 to 3%), the preloading procedure was terminated. Afterward, the samples were cooled down to RT for subsequent testing. An overestimation of specimen displacement during the compression test induced by a displacement associated with the measuring instrument (machine compliance) was systematically corrected.

Supplementary Materials

This PDF file includes:

Figs. S1 to S8
Table S1
Legends for movies S1 to S9

Other Supplementary Material for this manuscript includes the following:

Movies S1 to S9

REFERENCES AND NOTES

1. Z. H. Jia, X. U. Tang, D. G. Chen, J. B. Wu, Q. X. Liu, Magnetic properties and high thermal conductivity of Al_2O_3 ceramics prepared by spark plasma sintering. *Adv. Mat. Res.* **750-752**, 512–516 (2013).
2. X. Q. Cao, R. Vassen, D. Stoever, Ceramic materials for thermal barrier coatings. *J. Eur. Ceram. Soc.* **24**, 1–10 (2004).
3. O. L. Ighodaro, O. I. Okoli, Fracture toughness enhancement for alumina systems: A review. *Int. J. Appl. Ceram. Technol.* **5**, 313–323 (2008).
4. R. Danzer, T. Lube, P. Supancic, R. Damani, Fracture of ceramics. *Adv. Eng. Mater.* **10**, 275–298 (2008).
5. Y. Zheng, K. Zhang, T. T. Liu, W. H. Liao, C. D. Zhang, H. Shao, Cracks of alumina ceramics by selective laser melting. *Ceram. Int.* **45**, 175–184 (2019).
6. W. Sigle, C. Sarbut, D. Brunner, M. Rühle, Dislocations in plastically deformed $SrTiO_3$. *Phil. Mag.* **86**, 4809–4821 (2006).
7. Z. Mao, K. M. Knowles, Dissociation of lattice dislocations in $SrTiO_3$. *Phil. Mag.* **73**, 699–708 (1996).
8. T. Matsunaga, H. Saka, Transmission electron microscopy of dislocations in $SrTiO_3$. *Philos Mag Lett.* **80**, 597–604 (2000).
9. X. Fang, K. Ding, S. Janocha, C. Minnert, W. Rheinheimer, T. Frömling, K. Durst, A. Nakamura, J. Rödel, Nanoscale to microscale reversal in room-temperature plasticity in SrTiO3 by tuning defect concentration. *Scr. Mater.* **188**, 228–232 (2020).

10. J. Amodeo, S. Merkel, C. Tromas, P. Carrez, S. Korte-Kerzel, P. Cordier, J. Chevalier, Dislocations and plastic deformation in MgO crystals: A review. *Crystals* **8**, 240 (2018).
11. T. E. Mitchell, K. P. D. Lagerlöf, A. H. Heuer, Dislocations in ceramics. *Mater. Sci. Technol.* **1**, 944–949 (1985).
12. L. Porz, 60 years of dislocations in ceramics: A conceptual framework for dislocation mechanics in ceramics. *Int. J. Ceram. Eng. Sci.* **4**, 214–239 (2022).
13. P. Gumbsch, S. Taeri-Baghbadrani, D. Brunner, W. Sigle, M. Rühle, Plasticity and an inverse brittle-to-ductile transition in strontium titanate. *Phys. Rev. Lett.* **87**, 85505-1–85505–2 (2001).
14. X. Shi, H. Chen, F. Hao, R. Liu, T. Wang, P. Qiu, U. Burkhardt, Y. Grin, L. Chen, Room-temperature ductile inorganic semiconductor. *Nat. Mater.* **17**, 421–426 (2018).
15. J. Karch, R. Birringer, H. Gleiter, Ceramics ductile at low temperature. *Nature* **330**, 556–558 (1987).
16. F. Östlund, K. Rzepiejewska-Malyska, K. Leifer, L. M. Hale, Y. Tang, R. Ballarini, W. W. Gerberich, J. Michler, Brittle-to-ductile transition in uniaxial compression of silicon pillars at room temperature. *Adv. Funct. Mater.* **19**, 2439–2444 (2009).
17. J. Michler, K. Wasmer, S. Meier, F. Östlund, K. Leifer, Plastic deformation of gallium arsenide micropillars under uniaxial compression at room temperature. *Appl. Phys. Lett.* **90**, 043123 (2007).
18. F. Östlund, P. R. Howie, R. Ghisleni, S. Korte, K. Leifer, W. J. Clegg, J. Michler, Ductile-brittle transition in micropillar compression of GaAs at room temperature. *Phil. Mag.* **91**, 1190–1199 (2011).
19. S. Kiani, C. Ratsch, A. M. Minor, S. Kodambaka, J. M. Yang, Orientation- and size-dependent room-temperature plasticity in ZrC crystals. *Phil. Mag.* **95**, 985–997 (2015).
20. W. S. Rubink, V. Ageh, H. Lide, N. A. Ley, M. L. Young, D. T. Casem, E. J. Faierson, T. W. Scharf, Spark plasma sintering of B4C and B4C-TiB2 composites: Deformation and failure mechanisms under quasistatic and dynamic loading. *J. Eur. Ceram. Soc.* **41**, 3321–3332 (2021).
21. R. W. Rice, *Mechanical Properties of Ceramics and Composites: Grain And Particle Effects*, (2000).
22. Q. Tai, A. Mocellin, Review: High temperature deformation of Al2O3-based ceramic particle or whisker composites. *Ceram. Int.* **25**, 395–408 (1999).
23. J. Li, B. Cui, H. Wang, Y. Lin, X. Deng, M. Li, C. Nan, The effects of spark-plasma sintering (SPS) on the microstructure and mechanical properties of BaTiO3/3Y-TZP composites. *Materials* **9**, 320 (2016).
24. Z. Shen, M. Johnsson, Z. Zhao, M. Nygren, Spark plasma sintering of alumina. *J. Am. Ceram. Soc.* **85**, 1921–1927 (2002).
25. J. Liu, Y. Wang, F. Yang, K. Chen, L. An, Grain refining in spark plasma sintering Al2O3 ceramics. *J. Alloys Compd.* **622**, 596–600 (2015).
26. C. Wang, X. Wang, Z. Zhao, Microstructure homogeneity control in spark plasma sintering of Al2O3 ceramics. *J. Eur. Ceram. Soc.* **31**, 231–235 (2011).
27. S. Liu, R. Raghavan, X. T. Zeng, J. Michler, W. J. Clegg, Compressive deformation and failure of CrAlN/Si_3N_4 nanocomposite coatings. *Appl. Phys. Lett.* **104**, 081919 (2014).
28. K. R. Venkatachari, R. Raj, Superplastic flow in fine-grained alumina. *J. Am. Ceram. Soc.* **69**, 135–138 (1986).
29. C. Shen, T. Niu, B. Yang, J. Cho, Z. Shang, T. Sun, A. Shang, R. E. García, H. Wang, X. Zhang, Micromechanical properties and microstructures of AC and DC flash-sintered alumina. *Mater. Sci. Eng. A* **866**, 144631 (2023).
30. J. Cho, J. Li, H. H. Wang, Q. Li, Z. Fan, A. K. Mukherjee, W. Rheinheimer, H. H. Wang, X. Zhang, Study of deformation mechanisms in flash-sintered yttria-stabilized zirconia by in-situ micromechanical testing at elevated temperatures. *Mat. Res. Lett.* **7**, 194–202 (2019).
31. J. Cho, Q. Li, H. H. Wang, Z. Fan, J. Li, S. Xue, K. S. N. Vikrant, H. H. Wang, T. B. Holland, A. K. Mukherjee, R. E. García, X. Zhang, High temperature deformability of ductile flash-sintered ceramics via in-situ compression. *Nat. Commun.* **9**, 1 (2018).
32. J. Li, J. Cho, J. Ding, H. Charalambous, S. Xue, H. Wang, X. L. Phuah, J. Jian, X. Wang, C. Ophus, T. Tsakalakos, R. Edwin García, A. K. Mukherjee, N. Bernstein, C. Stephen Hellberg, H. Wang, X. Zhang, Nanoscale stacking fault–assisted room temperature plasticity in flash-sintered TiO2. *Sci. Adv.* **5**, eaaw5519 (2019).
33. X. L. Phuah, J. Cho, T. Tsakalakos, A. K. Mukherjee, H. Wang, X. Zhang, Defects in flash-sintered ceramics and their effects on mechanical properties. *MRS Bull.* **46**, 44–51 (2021).
34. W. Rheinheimer, X. Li Phuah, H. H. Wang, F. Lemke, M. J. Hoffmann, H. Wang, The role of point defects and defect gradients in flash sintering of perovskite oxides. *Acta Mater.* **165**, 398–408 (2019).
35. H. Wang, X. L. Phuah, J. Li, T. B. Holland, K. S. N. Vikrant, Q. Li, C. S. Hellberg, N. Bernstein, R. E. García, A. Mukherjee, X. Zhang, H. Wang, Key microstructural characteristics in flash sintered 3YSZ critical for enhanced sintering process. *Ceram. Int.* **45**, 1251–1257 (2019).
36. B. Yang, X. L. Phuah, Z. Shang, X. Sheng, H. Wang, X. Zhang, Effects of incubation on microstructure gradient in flash-sintered TiO_2. *Scr. Mater.* **207**, 114270 (2022).
37. M. Yu, S. Grasso, R. Mckinnon, T. Saunders, M. J. Reece, Review of flash sintering: Materials, mechanisms and modelling. *Adv. Appl. Ceram.* **116**, 24–60 (2017).
38. Y. Dong, I.-W. Chen, Predicting the onset of flash sintering. *J. Am. Ceram. Soc.* **98**, 2333–2335 (2015).
39. R. I. Todd, *Flash Sintering of Ceramics: A Short Review. Paper presented at Proceedings of the IV Advanced Ceramics and Applications Conference*. p 1–12, (2017).
40. H. Charalambous, S. K. Jha, H. H. Wang, X. L. Phuah, H. H. Wang, T. Tsakalakos, Inhomogeneous reduction and its relation to grain growth of titania during flash sintering. *Scr. Mater.* **155**, 37–40 (2018).
41. W. J. Clegg, Controlling cracks in ceramics. *Science* **286**, 1097–1099 (1999).
42. W. J. Clegg, K. Kendall, N. M. N. Alford, T. W. Button, J. D. Birchall, A simple way to make tough ceramics. *Nature.* **347**, 455–457 (1990).
43. S. Korte, W. J. Clegg, Micropillar compression of ceramics at elevated temperatures. *Scr. Mater.* **60**, 807–810 (2009).
44. T. E. Mitchell, Dislocations and mechanical properties of MgO-Al2O3 spinel single crystals *J. Am. Ceram. Soc.* 3305–810 (1999).
45. K. P. D. Lagerlöf, A. H. Heuer, J. Castaing, J. P. Rivière, T. E. Mitchell, Slip and twinning in sapphire (α-Al_2O_3). *J. Am. Ceram. Soc.* **77**, 385–397 (1994).
46. S. Takeuchi, T. Hashimoto, Deformation mechanisms in titanium dioxide single crystals. *J. Mater. Sci.* **25**, 417–423 (1990).
47. K. H. G. Ashbee, R. E. Smallman, Stress-strain behavior of titanium dioxide (rutile) single crystals. *J. Am. Ceram. Soc.* **46**, 211–214 (1963).
48. J. Castaing, A. Muñoz, D. Gomez Garcia, A. Dominguez Rodriguez, Basal slip in sapphire (α-Al2O3). *Mater. Sci. Eng. A* **233**, 121–125 (1997).
49. E. Tochigi, B. Miao, A. Nakamura, N. Shibata, Y. Ikuhara, Atomic-scale mechanism of rhombohedral twinning in sapphire. *Acta Mater.* **216**, 117137 (2021).
50. K. P. D. Lagerlof, B. J. Pletka, T. E. Mitchell, A. H. Heuer, Deformation and diffusion in sapphire (α-Al_2O_3). *Radiat. Eff.* **74**, 87–107 (2006).
51. A. H. Heuer, K. P. D. Lagerlöf, J. Castaing, Slip and twinning dislocations in sapphire (α-Al_2O_3). *Phil. Mag. A.* **78**, 747–763 (1998).
52. J. Castaing, A. He, K. P. D. Lagerlöf, A. H. Heuer, Deformation of sapphire (α-Al2O3) by basal slip and basal twinning below 700°C. *Phil. Mag.* **84**, 1113–1125 (2004).
53. A. Montagne, S. Pathak, X. Maeder, J. Michler, Plasticity and fracture of sapphire at room temperature: Load-controlled microcompression of four different orientations. *Ceram. Int.* **40**, 2083–2090 (2014).
54. P. Pirouz, B. F. Lawlor, T. Geipel, J. B. Bilde-Sørensen, A. H. Heuer, K. P. D. Lagerlöf, On basal slip and basal twinning in sapphire (α-Al2O3)—II. A new model of basal twinning. *Acta Mater.* **44**, 2153–2164 (1996).
55. W. G. Mao, Y. G. Shen, C. Lu, Nanoscale elastic–plastic deformation and stress distributions of the C plane of sapphire single crystal during nanoindentation. *J. Eur. Ceram. Soc.* **31**, 1865–1871 (2011).
56. J. Castaing, J. Cadoz, S. H. Kirby, Deformation of Al_2O_3 single crystals between 25°C and 1800°C: Basal and prismatic slip. *J. Phys. Colloq.* **42**, C3-43–C3-47 (1981).
57. R. Su, D. Neffati, Y. Zhang, J. Cho, J. Li, H. Wang, Y. Kulkarni, X. Zhang, The influence of stacking faults on mechanical behavior of advanced materials. *Mater. Sci. Eng. A* **803**, 140696 (2021).
58. R. Su, D. Neffati, J. Cho, Z. Shang, Y. Zhang, J. Ding, Q. Li, S. Xue, H. Wang, Y. Kulkarni, X. Zhang, High-strength nanocrystalline intermetallics with room temperature deformability enabled by nanometer thick grain boundaries. *Sci. Adv.* **7**, eabc8288 (2021).
59. D. Bufford, Y. Liu, J. Wang, H. Wang, X. Zhang, In situ nanoindentation study on plasticity and work hardening in aluminium with incoherent twin boundaries. *Nat. Commun.* **5**, 4864 (2014).
60. L. Lu, Z. S. You, K. Lu, Work hardening of polycrystalline Cu with nanoscale twins. *Scr. Mater.* **66**, 837–842 (2012).
61. K. Lu, L. Lu, S. Suresh, Strengthening materials by engineering coherent internal boundaries at the nanoscale. *Science* **324**, 349–3652 (2009).
62. Y. Liu, J. Song, G. Liu, J. Chen, C. Wang, H. Wang, J. Wang, X. Zhang, High strength and low coercivity of cobalt with three-dimensional nanoscale stacking faults. *Nano Lett.* **21**, 6480–6486 (2021).
63. M. Dao, L. Lu, Y. F. Shen, S. Suresh, Strength, strain-rate sensitivity and ductility of copper with nanoscale twins. *Acta Mater.* **54**, 5421–5432 (2006).
64. E. Ma, Y. M. Wang, Q. H. Lu, M. L. Sui, L. Lu, K. Lu, Strain hardening and large tensile elongation in ultrahigh-strength nano-twinned copper. *Appl. Phys. Lett.* **85**, 4932–4934 (2004).
65. L. Lu, Y. Shen, X. Chen, L. Qian, K. Lu, Ultrahigh strength and high electrical conductivity in copper. *Science* **304**, 422–426 (2004).
66. L. Lu, X. Chen, X. Huang, K. Lu, Revealing the maximum strength in nanotwinned copper. *Science* **323**, 607–610 (2009).
67. T. Zhu, J. Li, A. Samanta, H. G. Kim, S. Suresh, Interfacial plasticity governs strain rate sensitivity and ductility in nanostructured metals. *Proc. Natl. Acad. Sci. U.S.A.* **104**, 3031–3036 (2007).
68. N. Li, J. Wang, S. Mao, H. Wang, In situ nanomechanical testing of twinned metals in a transmission electron microscope. *MRS Bull.* **41**, 305–313 (2007).

69. R. Su, D. Neffati, J. Cho, Q. Li, J. Ding, H. Wang, Y. Kulkarni, X. Zhang, Phase transformation induced plasticity in high-strength hexagonal close packed Co with stacking faults. *Scr. Mater.* **173**, 32–36 (2019).
70. V. Trabadelo, S. Pathak, F. Saeidi, M. Parlinska-Wojtan, K. Wasmer, Nanoindentation deformation and cracking in sapphire. *Ceram. Int.* **45**, 9835–9845 (2019).
71. X. Fang, K. Ding, C. Minnert, A. Nakamura, K. Durst, Dislocation-based crack initiation and propagation in single-crystal SrTiO3. *J. Mater. Sci.* **56**, 5479–5492 (2021).
72. J. B. Wachtman, W. R. Cannon, M. J. Matthewson, *Mechanical Properties of Ceramics* (Wiley, ed. 2, 2009).
73. W. D. Scott, K. K. Orr, Rhombohedral twinning in alumina. *J. Am. Ceram. Soc.* **66**, 27–32 (1983).
74. T. Geipel, K. P. D. Lagerlöf, P. Pirouz, A. H. Heuer, A zonal dislocation mechanism for rhombohedral twinning in sapphire (α-Al_2O_3). *Acta Metallurgica Et Materialia.* **42**, 1367–1372 (1994).
75. Y. Morris Wang, F. Sansoz, T. Lagrange, R. T. Ott, J. Marian, T. W. Barbee, A. V. Hamza, Defective twin boundaries in nanotwinned metals. *Nat. Mater.* **12**, 697–702 (2013).
76. J. Wang, N. Li, O. Anderoglu, X. Zhang, A. Misra, J. Y. Huang, J. P. Hirth, Detwinning mechanisms for growth twins in face-centered cubic metals. *Acta Mater.* **58**, 2262–2270 (2010).
77. E. Ma, T. Zhu, Towards strength–ductility synergy through the design of heterogeneous nanostructures in metals. *Mater. Today* **20**, 323–331 (2017).
78. F. Duan, Y. Lin, J. Pan, L. Zhao, Q. Guo, D. Zhang, Y. Li, Ultrastrong nanotwinned pure nickel with extremely fine twin thickness. *Sci. Adv.* **7**, eabg5113 (2021).
79. Y. T. Zhu, X. Z. Liao, X. L. Wu, Deformation twinning in nanocrystalline materials. *Prog Mater Sci.* **57**, 1–62 (2012).
80. N. Li, J. Wang, A. Misra, X. Zhang, J. Y. Huang, J. P. Hirth, Twinning dislocation multiplication at a coherent twin boundary. *Acta Mater.* **59**, 5989–5996 (2011).
81. N. Li, J. Wang, J. Y. Huang, A. Misra, X. Zhang, Influence of slip transmission on the migration of incoherent twin boundaries in epitaxial nanotwinned Cu. *Scr. Mater.* **64**, 149–152 (2011).
82. W. G. Mao, Y. G. Shen, C. Lu, Deformation behavior and mechanical properties of polycrystalline and single crystal alumina during nanoindentation. *Scr. Mater.* **65**, 127–130 (2011).
83. J. Wang, L. Liu, C. N. Tomé, S. X. Mao, S. K. Gong, C. J. Wang, Twinning and de-twinning via glide and climb of twinning dislocations along serrated coherent twin boundaries in hexagonal-close-packed metals. *Mater. Res. Lett.* **1**, 81–88 (2013).
84. S. Lee, J. Im, Y. Yoo, E. Bitzek, D. Kiener, G. Richter, B. Kim, S. H. Oh, Reversible cyclic deformation mechanism of gold nanowires by twinning–detwinning transition evidenced from in situ TEM. *Nat. Commun.* **5**, 3033 (2014).
85. N. Lu, K. Du, L. Lu, H. Q. Ye, Transition of dislocation nucleation induced by local stress concentration in nanotwinned copper. *Nat. Commun.* **16**, 7648 (2015).
86. Z. W. Shan, R. K. Mishra, S. A. Syed Asif, O. L. Warren, A. M. Minor, Mechanical annealing and source-limited deformation in submicrometre-diameter Ni crystals. *Nat. Mater.* **7**, 115–119 (2007).
87. Y. Gao, Z. L. Liu, Z. Zhuang, The investigation of size effect for dislocation starvation mechanism under Cu single-crystal micro-pillar compression. *AIP Conf. Proc.* **1233**, 436–441 (2010).
88. W. D. Nix, J. R. Greer, G. Feng, E. T. Lilleodden, Deformation at the nanometer and micrometer length scales: Effects of strain gradients and dislocation starvation. *Thin Solid Films* **515**, 3152–3157 (2007).
89. J. R. Greer, W. D. Nix, Nanoscale gold pillars strengthened through dislocation starvation. *Phy. Rev. B.* **73**, 245410 (2006).
90. P. Hirel, M. Mrovec, C. Elsässer, Atomistic simulation study of ⟨1 1 0⟩ dislocations in strontium titanate. *Acta Mater.* **60**, 329–338 (2012).
91. N. Shibata, M. F. Chisholm, A. Nakamura, S. J. Pennycook, T. Yamamoto, Y. Ikuhara, Nonstoichiometric dislocation cores in α-alumina. *Science* **316**, 82–85 (2007).
92. Y. Liu, X. Cui, R. Niu, S. Zhang, X. Liao, S. D. Moss, P. Finkel, M. Garbrecht, S. P. Ringer, J. M. Cairney, Giant room temperature compression and bending in ferroelectric oxide pillars. *Nat. Commun.* **13**, 335 (2022).

Acknowledgments: We would like to acknowledge access to the Life Science Microscopy Facility and the microscopy center of the School of Materials Engineering at Purdue University. **Funding:** The work is supported by the US Office of Naval Research (contract nos. N00014-17-1-2087 and N00014-22-1-2160 for sintering effort and N00014-20-1-2043 for TEM). The ASTAR crystal orientation system in the TEM microscope is supported by ONR-DURIP DURIP project number N00014-20-1-2659. A provisional patent is in preparation. **Author contributions:** Conceptualization: C.S., J.L., H.W., and X.Z. Methodology: C.S. and J.L. Investigation: C.S., J.L., T.N., J.C., Z.S., Y.Z., A.S., B.Y., and K.X. Supervision: X.Z., H.W., and R.E.G. Writing—original draft: C.S. Writing—review and editing: C.S., J.C., X.Z., and H.W. **Competing interests:** The authors declare that they have no competing interests. **Data and materials availability:** All data needed to evaluate the conclusions in the paper are present in the paper and/or the Supplementary Materials.

Submitted 25 June 2023
Accepted 15 March 2024
Published 17 April 2024
10.1126/sciadv.adj4079